



ModusGraph: Automated 3D and 4D Mesh Model Reconstruction from Cine CMR with Improved Accuracy and Efficiency

Yu Deng¹, Hao Xu¹, Sashya Rodrigo¹, Steven E. Williams^{1,2},
Michelle C. Williams², Steven A. Niederer¹, Kuberan Pushparajah¹,
and Alistair Young^{1(✉)}

¹ School of Biomedical Engineering and Imaging Sciences,
King's College London, London, UK
alistair.young@kcl.ac.nz

² University/BHF Centre for Cardiovascular Science,
University of Edinburgh, Edinburgh, UK

Abstract. Anatomical heart mesh models created from cine cardiac images are useful for the evaluation and monitoring of cardiovascular diseases, but require challenging and time-consuming reconstruction processes. Errors due to reduced spatial resolution and motion artefacts limit the accuracy of 3D models. We proposed ModusGraph to produce a higher quality 3D and 4D (3D+time) heart models automatically, employing i) a voxel processing module with Modality Handles and a super-resolution decoder to define low-resolution and high-resolution segmentations and correct motion artefacts with multi-modal unpaired data, ii) a Residual Spatial-temporal Graph Convolution Network to generate mesh models by controlled and progressive spatial-temporal deformation to better capture the cardiac motion, and iii) a Signed Distance Sampling process to bridge those two parts for end-to-end training. ModusGraph was trained and evaluated on CT angiograms and cardiovascular MRI cines, showing superior performance compared to other mesh reconstruction methods. It creates well-defined meshes from sparse MRI cines, enabling vertex tracking across cardiac cycle frames. This process aids in analyzing myocardium function and conducting biomechanical analyses from imaging data <https://github.com/MalikTeng/ModusGraph>.

Keywords: Cardiovascular Magnetic Resonance · 3D heart model · Motion Artefacts · Super-resolution · Graph Neural Network

Supplementary Information The online version contains supplementary material available at https://doi.org/10.1007/978-3-031-43990-2_17.

1 Introduction

Multi-slice cine cardiovascular magnetic resonance (CMR) scanning is a common method for the accurate diagnosis and evaluation of cardiovascular diseases [16, 25]. Although this provides a series of images of the heart and blood vessels over time, it is often a lengthy process that obtains only certain slices of the heart which limit the visualization of certain structures, and has breath-hold motion artefacts resulting in misalignment between slices

To better evaluate heart disease, plan interventions, and monitor heart disease, a 3D heart model can be created from cine CMRs, which is a digitized heart object visualized as triangular meshes [9]. This reconstruction is accomplished in several steps: segmentation, registration, reconstruction, refinement, and visualisation. Because of the time cost and expert knowledge required for this task, it is desirable to create 3D or 4D (3D+time) heart models automatically for every patient [3, 23]. However, it is challenging to create accurate 3D heart models, because of the impact of low spatial resolution and motion artefacts [11, 18].

To this end, we proposed a Recurrent Graph Neural Network based method, ModusGraph, to fully automate the reconstruction of 4D heart models from cine CMR. This includes i) a voxel processing module with Modality Handles (Modhandle) and ResNet decoder for super-resolution and correction of motion artefacts from the acquired cine CMR, ii) a Residual Spatial-temporal Graph Convolution module (R-StGCN) for 4D mesh models generation by hierarchically spatial deformation and temporal motion estimation, and iii) a Signed Distance Sampling process bridge voxel features from segmentation and vertex features from deformation.

2 Related Works

Surface meshing involves constructing polygonal representations of geometric objects or surfaces, and creating high-quality and feature-aware surface meshes for medical imaging applications it is of particular interest.

With available large-volume training data and advanced computational resources, more studies harness the strength of deep learning and traditional methods to avoid user supervision. Aubert et al. [2] use convolutional neural networks to automatically detect anatomical landmarks for spine reconstruction. Ma et al. [22] propose a dense SLAM technique for colon surface reconstruction. Gopinath et al. [7] presented SegRecon, an end-to-end deep learning approach that for simultaneous reconstruction and segmentation of cortical surfaces directly from an MRI volume. Wang et al. [26] reconstructed 3D surfaces from 2D images using a neural network that learns a Signed Distance Function (SDF) representation from 2D images. Ma et al. [21] proposed a deep learning framework that uses neural ordinary differential equations (ODEs) for efficient cortical surface reconstruction from brain MRI scans. Similarly, Lebrat et al. [17] presents CorticalFlow, a geometric deep learning model that learns to deform a reference template mesh towards a targeted object in a 3D image, by solving ODEs from stationary velocity fields.

In contrast to those methods applying directly to the surface manifold, others, similar to our method, combine image segmentation with explicit surface representations and mesh deformation with coarse to fine controls. Wickramasinghe et al. [27] introduced Voxel2Mesh, a two-stage method that uses a CNN for voxel labelling and a GCN for mesh generation. Bongratz et al. [4] presented a deep learning algorithm that reconstructs explicit meshes of cortical surfaces from brain MRI scans using a convolutional and graph neural network, resulting in four meshes. Kong et al. [14] proposed a method that generates simulation-ready meshes of cardiac structures using atlas-based registration and shape-preserving interpolation. They also introduced a deep learning approach that constructs whole heart meshes by learning to deform a small set of deformation handles on a whole heart template [15]. Here, we utilize sparse CMRs to generate temporally coherent dynamic meshes for the cardiac cycle, leveraging unpaired high-resolution CT datasets (Fig. 1). These meshes are geometrically and topologically well-defined, with trackable vertices across consecutive frames. Such features enhance the analysis of myocardium function and enable biomechanical computational analysis (e.g., for stiffness or contractility estimation from finite element analysis of imaging data).

3 Method

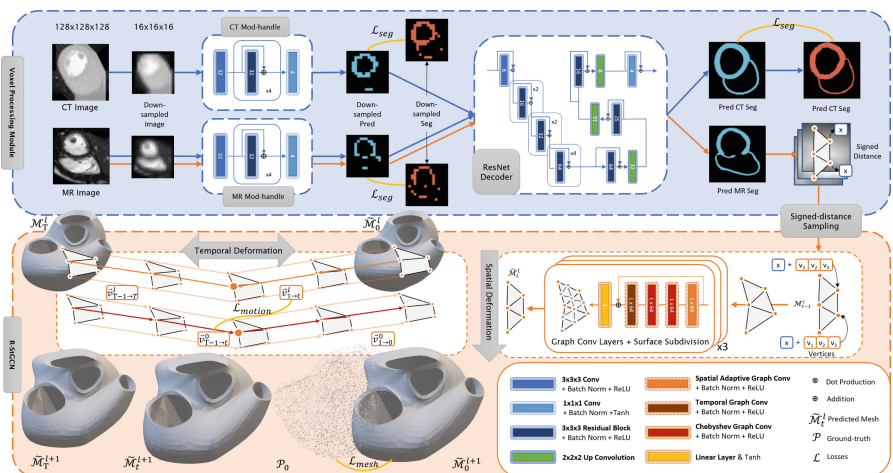


Fig. 1. Schematic of ModusGraph. It consists of two main components: a voxel processing module to generate high-resolution segmentations from image volumes, and an R-StGCN module based on a graph convolution network that deforms an initial coarse mesh progressively and dynamically by frames. A Signed Distance Sampling procedure bridges those two parts for end-to-end training.

3.1 Voxel Processing Module

Modality Handles. Compared to cine CMRs, CT imaging provides higher spatial resolution and enables easier high-resolution segmentation of the heart. The developed network to generate such segmentation is transferable to process cine CMRs, allowing for comparable cardiac structural information to be extracted from similar patient populations. The following module is thus proposed to estimate high-resolution segmentations from unpaired CT and cine CMR image volumes. An input image volume $X_{CT} \in \mathbb{R}^{H \times W \times D}$ is cropped around the anatomy of interest to the size of $128 \times 128 \times 128$, and then down-sampled following bilinear interpolation method to $X'_{CT} \in \mathbb{R}^{16 \times 16 \times 16}$, which enables a common low-resolution segmentation space for cine CMRs. Its predicted segmentation $\tilde{Y}'_{CT} \in \mathbb{R}^{16 \times 16 \times 16}$ is generated by a CT Modality Handle (CT Mod-handle, $h(X_{CT})$), using ResNet blocks followed by ReLU non-linear activity and a one-by-one convolution layer. A MR Modality Handle (MR Mod-handle, $h(X_{MR})$) generates predicted segmentation \tilde{Y}_{MR} from cine CMRs in the same way.

Super-Resolution Decoder. \tilde{Y}'_{CT} is passed to a decoder for super-resolution reconstruction to a size of $128 \times 128 \times 128$. The decoder ψ includes three layers of up convolution followed by ResNet blocks. The high-resolution segmentation of cine CMR is generated similarly through $\tilde{Y}_{MR} = \mathbf{W}_\psi \mathbf{W}_h X_{MR}$, where \mathbf{W}_ψ and \mathbf{W}_h are trainable weights of decoder and Mod-handle, respectively. To include heart morphological features in the graph convolution process, the signed distance is calculated from the decoder’s output. This signed distance is computed as geodesic distances from each voxel to the surface boundary [1, 5]. The mesh is then scaled to the output size and each mesh surface vertex is assigned a signed distance based on the output channel and vertex’s coordinates.

3.2 Residual Spatial-Temporal Graph Convolution Module (R-StGCN)

Graph convolution networks can be utilized to reshape a heart mesh model, but regressing the surface near sharp edges or areas with aggressive Laplacian changes is challenging due to the networks’ lack of awareness of the position relationships. We borrowed the idea of graph construction from human joints to overcome this issue [30]. The area of the 1-connected neighbourhood near sharp edges is divided into 3 subsets k : one subset includes vertices on the valves’ edges, and the other two subsets include vertices on different sides of the myocardium surfaces. This defines the robust position relationships of sharp edges and other convex areas of the mesh, allowing us to use Adaptive Graph Convolutional (AGC) layers [24] to learn such relationships.

Spatial Deformation. Given a dynamic mesh at level l and frame t , i.e. $\mathcal{M}_t^l = (\mathcal{V}_t^l, \mathcal{E}_t^l)$, where \mathcal{V}_t^l and \mathcal{E}_t^l are N vertices and M edges, respectively. A dense adjacency matrix $\mathbf{A}_k \in \mathbb{R}^{N \times N}$ denotes the edges between every two vertices.

A data-dependent matrix $\mathbf{C}_k \in \mathbb{R}^{N \times N}$ determines the similarity of every two vertices as normalized Gaussian function, $\mathbf{C}_k = \text{softmax}(f_{in}^T \mathbf{W}_{\theta k}^T \mathbf{W}_{\phi k} f_{in})$. $\mathbf{W}_{\theta k}$ and $\mathbf{W}_{\phi k}$ are the parameters of the 1×1 convolution layer θ and ϕ , respectively. $f_{in} \in \mathbb{R}^{3 \times T \times N}$ is input feature matrix of the convolution layer, where T is the number of frames for each cardiac cycle. The sampling area of convolution is a 1-connected neighbourhood includes 3 subsets, which conforms with the aforementioned mesh topology. It is described as $f_{out} = \sum_{k=1}^{K=3} \mathbf{W}_k f_{in} (\mathbf{A}_k + \mathbf{C}_k)$. f_{out} is output feature of the convolution layer, \mathbf{W}_k is trainable weights for the convolution. Following the AGC layer, we used graph convolution with first-order Chebyshev polynomial approximation. It is formalized as $f_{out} = \sigma(\mathbf{W}_{\theta 0} f_{in} + \mathbf{W}_{\theta 1} f_{in} \tilde{\mathbf{L}})$, where $\mathbf{W}_{\theta 0}, \mathbf{W}_{\theta 1}$ are trainable weights and $\tilde{\mathbf{L}} = 2\mathbf{L}_{norm}/\lambda_{max} - \mathbf{I}$, $\tilde{\mathbf{L}} \in \mathbb{R}^{N \times N}$ is the scaled and normalized Laplacian matrix [6]. The signed distance was added to mesh vertices prior to the graph convolution, and a straightforward Loop method [19] for surface subdivision is applied to refine the coarse mesh.

Temporal Deformation. The deformation field vector $\vec{\mathcal{V}}_{t-1 \rightarrow t}$ and $\vec{\mathcal{V}}_{t \rightarrow t-1}$ are learnt through temporal convolutions, where the sampling neighbourhood is defined as a vertex in consecutive frames. It is a $T \times 1$ convolution performed on the output feature matrix f_{out} in a bidirectional manner. $\vec{\mathcal{V}}$ is regularized following the principle of motion estimation. With vertices of meshes at consecutive frames \mathcal{V}_0 and \mathcal{V}_1 , the vertices of intermediate mesh $\mathcal{V}_t, 0 < t < 1$ is approximated under symmetric assumption [28], as $\tilde{\mathcal{V}}_t = 0.5 \cdot (t \cdot (\mathcal{V}_0 + t \cdot \vec{\mathcal{V}}_{0 \rightarrow 1}) + (1-t) \cdot (\mathcal{V}_1 + (1-t) \cdot \vec{\mathcal{V}}_{1 \rightarrow 0}))$, and we measure the L1 difference between $\tilde{\mathcal{V}}_t$ and \mathcal{V}_t .

3.3 Training Scheme

Generally, the MR Mod-handle was trained on cine CMRs and down-sampled segmentation, described as $\mathcal{L}_{seg,MR}(h(\mathbf{X}_{MR}), \mathbf{Y'}_{MR})$. The CT Mod-handle and ResNet decoder were trained on CT image volumes, segmentation and their down-sampled counterparts using dice loss and cross-entropy loss, i.e. $\mathcal{L}_{seg,CT}(\psi \cdot h(\mathbf{X}_{CT}), \mathbf{Y}_{CT}, \mathbf{Y'}_{CT})$. Supervised by the ground-truth point clouds from CT segmentation, meshes were predicted from the R-StGCN module, where Chamfer distance is minimized together with surface regularization [27] and deformation field vector regularization as $\mathcal{L}_{mesh,CT} = \sum_{t=0}^{T=1} \sum_{l=0}^{L=2} \text{dCD}(\tilde{\mathcal{M}}_t^l, \mathcal{P}_t) + \lambda_{reg} \cdot (\mathcal{L}_{regular}(\mathcal{M}_t^l) + \|\tilde{\mathcal{V}}_t^l - \mathcal{V}_t^l\|_1)$. \mathcal{P}_t was generated via Marching Cubes [20] and uniform surface sampling applied to the ground-truth segmentation. Similarly, pseudo point clouds $\tilde{\mathcal{P}}_t$ from super-resolved cine CMRs segmentation were used for fine-tuning the R-StGCN module, i.e. $\mathcal{L}_{mesh,MR}$. The total loss is $\mathcal{L}_{total} = \lambda_{seg} \cdot (\mathcal{L}_{seg,CT} + \mathcal{L}_{seg,MR}) + \lambda_{mesh} \cdot (\mathcal{L}_{mesh,CT} + \mathcal{L}_{mesh,MR})$, where $\lambda_{seg} = 0.5$, $\lambda_{mesh} = 1.0$ and $\lambda_{reg} = 0.1$ were selected by extensive experiments from $[0, 1]$. Find a detailed training/testing scheme in Appendix V. ModusGraph is implemented with PyTorch 1.12.1 and the experiment was conducted on an RTX 3090 GPU, with Adam optimizer and a learning rate of $1e-4$. The training and validation losses converge after 200 epochs in less than 2 h.

4 Results and Discussion

4.1 Datasets

The training and validation data consisted of CT image volumes from the SCOT-HEART study [12] and cine CMRs from the Cardiac Atlas Project (CAP) tetralogy of Fallot [8] database. CT data were included to provide high-resolution geometry information while tetralogy of Fallot CMR cases were used because functional analyses are important for these patients. The SCOT-HEART dataset provided 400 and 200 image volumes for training and testing, while the CAP dataset provided 84 and 48 time-series image volumes for training and testing. Data augmentation techniques included random intensity shifting, scaling, contrast adjustment, random rotation, and intensity normalization. Ground-truth segmentations of four heart chambers, left ventricle myocardium, and aorta artery from a previously validated method [29] was used for the whole heart meshing on the SCOT-HEART dataset while left and right ventricle and myocardium manual segmentations were used for the dynamic meshing with the CAP dataset.

4.2 Evaluation of Whole Heart Meshes Quality

Table 1. Comparison of accuracy of generated mesh on SCOT-HEART test cases. Dice (decimal) and INTersection (percentage) scores were derived on voxelized meshes and ASD (decimal) is evaluated on meshes. Compared methods include Voxel2Mesh (VM), CorticalFlow (CF), nnU-Net3D+Point2Mesh (NNP), ResNet Decoder+Marching Cubes (RES) and ModusGraph (MG).

Metrics	Methods	LV	LV-MYO	RV	LA	RA	AV
Dice	VM (6k)	0.66 ± 0.11	0.35 ± 0.13	0.63 ± 0.12	0.54 ± 0.16	0.58 ± 0.13	0.47 ± 0.17
	CF (6k)	0.75 ± 0.08	0.50 ± 0.12	0.73 ± 0.08	0.67 ± 0.12	0.72 ± 0.10	0.61 ± 0.13
	NNP (6k)	0.75 ± 0.05	0.49 ± 0.08	0.72 ± 0.07	0.66 ± 0.04	0.70 ± 0.05	0.58 ± 0.06
	RES (14k)	0.92 ± 0.02	0.82 ± 0.05	0.91 ± 0.03	0.89 ± 0.03	0.90 ± 0.04	0.87 ± 0.05
	MG (6k)	0.77 ± 0.08	0.51 ± 0.13	0.75 ± 0.09	0.68 ± 0.11	0.73 ± 0.09	0.65 ± 0.14
ASD	VM (6k)	3.20e-01	5.88e-01	1.14e-01	1.89e-01	3.21e-01	1.31e+00
	CF (6k)	1.13e-02	8.24e-03	1.17e-02	1.64e-02	1.27e-02	1.40e-02
	NNP (6k)	1.16e-02	9.78e-03	1.21e-02	1.75e-02	1.46e-02	1.57e-02
	RES (14k)	1.01e-03	8.65e-04	1.45e-03	1.76e-03	1.81e-03	1.48e-03
	MG (6k)	1.06e-02	8.60e-03	1.09e-02	1.64e-02	1.18e-02	1.16e-02
INT	VM (6k)	15.74 ± 7.62	16.25 ± 5.82	9.16 ± 8.09	6.00 ± 8.41	7.57 ± 9.95	5.16 ± 8.86
	CF (6k)	12.34 ± 5.45	15.29 ± 9.81	11.77 ± 10.22	9.35 ± 6.38	6.42 ± 6.47	8.61 ± 7.31
	NNP (6k)	1.85 ± 0.96	2.24 ± 1.27	0.62 ± 0.42	0.25 ± 0.86	0.20 ± 0.32	0.18 ± 0.13
	RES (14k)	0.00 ± 0.00					
	MG (6k)	1.79 ± 0.68	2.39 ± 0.49	1.17 ± 0.14	0.43 ± 0.29	0.18 ± 0.10	1.50 ± 1.80

We evaluated the quality of meshes generated by ModusGraph, by comparing them to those produced by other state-of-the-art methods using the SCOT-HEART dataset. ModusGraph, Voxel2Mesh [27], and CorticalFlow [17] started

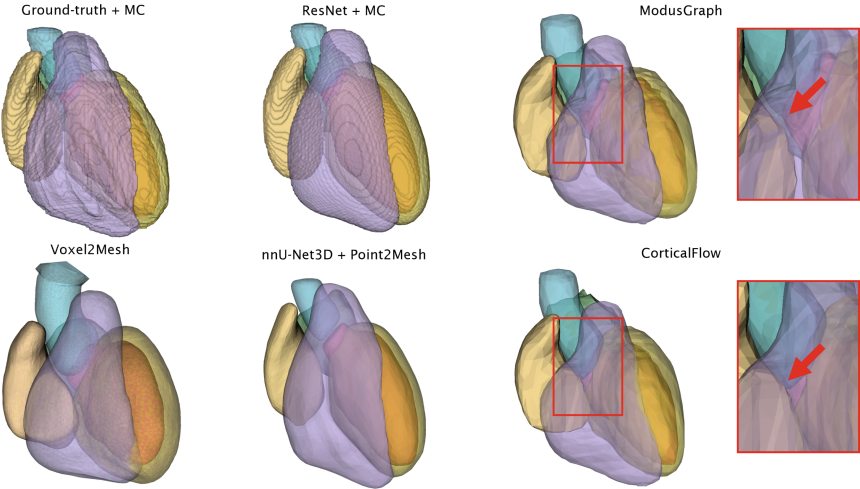


Fig. 2. Visualized meshes for a SCOT-HEART case. Arrows pointing to intersection structures in CorticalFlow

from the same template mesh and progressively deformed it to a finer mesh using $128 \times 128 \times 128$, while nnU-Net [13] segmentation and Point2Mesh [10] reconstruction used a user controlled, differentiable refinement process to warp the segmentation boundary point clouds to meshes. These methods produce meshes with around 6,000 vertices for each anatomy. The Marching Cubes method was also applied to the ResNet decoder’s segmentation to generate a finer mesh with around 14,000 vertices for evaluation. All methods for generating meshes had training times ranging from 2–5 hours.

Regarding the Dice score and Average Surface Distance (ASD) in Table 1, RES is a high benchmark since it was straightforward to reconstruct a high-resolution marching cubes mesh from the well-defined morphologies in the segmentations, but this is not suitable for tracking or computational models. ModusGraph’s mesh accuracy is compromised due to information loss in the QuickHull-derived template mesh (Appendix I), alignment issues with deformed meshes and segmentation in different coordinate systems, and difficulties in capturing patient-specific geometric variations. However, refining the template mesh and registration process could potentially enhance the results. Figure 2 and the intersection scores in Table 1 that measure the ratio of surface collision show that ModusGraph can generate accurate whole-heart meshes with less surface distortion and collision when compared to its closest result from CorticalFlow.

4.3 Dynamic Mesh for Biomechanical Simulation

We evaluated ModusGraph and other methods on the task of creating dynamic ventricle myocardium meshes. When them to ground-truth short-axis slices segmentation, the Average Surface Distance (ASD) at end-diastole (ED) and

Table 2. Comparison of quality of generated mesh on CAP test cases. Numbers are decimal except for Angle in degree.

	ASD	Aspect Ratio	Angle (min, max)	Jacobian
Voxel2Mesh	1.08e-1	1.55 ± 0.08	(37.21, 91.01)	0.72 ± 0.03
CorticalFlow	8.21e-2	1.62 ± 0.15	(31.77, 94.57)	0.69 ± 0.04
ModusGraph	5.14e-2	1.35 ± 0.00	(41.75, 81.21)	0.76 ± 0.00

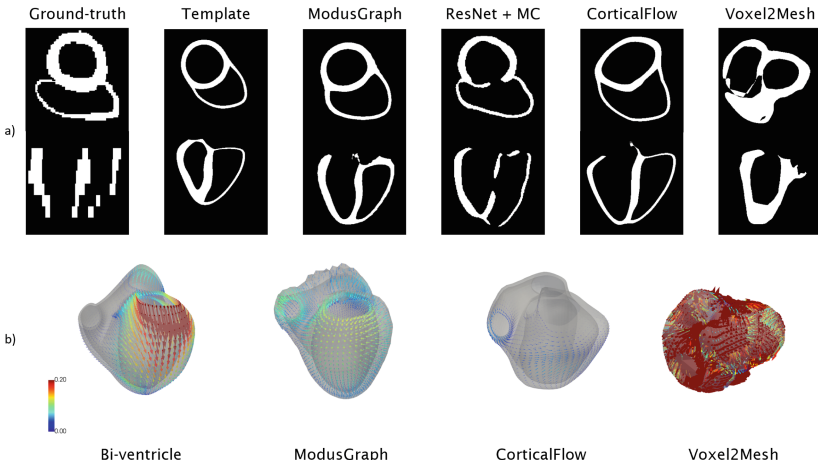


Fig. 3. Visualization of generated dynamic meshes' a) silhouette on short- and long-axis b) surface displacement between end-diastole and end-systole.

end-systole phases (ES) were used for evaluation since ground-truth dynamic meshes for each patient are challenging to obtain. ModusGraph more accurately deformed the template mesh towards true anatomy per patient, as shown by the silhouette of the generated meshes at ED in Fig 3-a. Generated meshes from nnUNet + Point2Mesh or ResNet + MC are not suitable for mechanical simulations without proper post-processing and were thus not compared to ModusGraph, Voxel2Mesh, and CorticalFlow.

Mesh quality for biomechanical simulations, including aspect ratio, min and max angle, and Jacobian of surface mesh triangular cells, was also evaluated. ModusGraph showed less distorted cells, leading to faster convergence for mechanical simulations, as shown in Table 2. Changes in mesh surface from ED to ES phase were compared to a reference dynamic mesh, Bi-ventricle [8], and ModusGraph was found to more accurately describe the deformation in areas surrounding valves and the displacement of the myocardium surface, as shown in Fig 3-b. The dynamic mesh generated by ModusGraph is included in supplementary materials, along with details for creating template meshes for the two tasks and reference Bi-ventricle mesh.

5 Conclusion

Our proposed method, ModusGraph, automates 4D heart model reconstruction from cine CMR using a voxel processing module, a Residual Spatial-temporal Graph Convolution module and a Signed Distance Sampling process. ModusGraph outperforms other state-of-the-art methods in reconstructing accurate 3D heart models from high-resolution segmentations on computed tomography images, and generates 4D heart models suitable for biomechanical analysis, which will aid in the understanding of congenital heart disease. This approach offers an efficient and automated solution for creating 3D and 4D heart models, with potential benefits for heart disease assessment, intervention planning, and monitoring.

Acknowledgements. YD was funded by the Kings-China Scholarship Council PhD Scholarship Program. HX was funded by Innovate UK (104691) London Medical Imaging & Artificial Intelligence Centre for Value Based Healthcare. SCOT-HEART was funded by The Chief Scientist Office of the Scottish Government Health and Social Care Directorates (CZH/4/588), with supplementary awards from Edinburgh and Lothian's Health Foundation Trust and the Heart Diseases Research Fund. AAY and KP acknowledge funding from the National Institutes of Health R01HL121754 and Wellcome ESPCR Centre for Medical Engineering at King's College London WT203148/Z/16/Z.

References

1. Asad, M., Dorent, R., Vercauteren, T.: Fastgeodis: fast generalised geodesic distance transform. *J. Open Sourc. Softw.* **7**(79), 4532 (2022)
2. Aubert, B., Vazquez, C., Cresson, T., Parent, S., de Guise, J.A.: Toward automated 3d spine reconstruction from biplanar radiographs using CNN for statistical spine model fitting. *IEEE Trans. Med. Imaging* **38**(12), 2796–2806 (2019)
3. Banerjee, A., et al.: A completely automated pipeline for 3d reconstruction of human heart from 2d cine magnetic resonance slices. *Phil. Trans. R. Soc. A* **379**(2212), 20200257 (2021)
4. Bongratz, F., Rickmann, A.M., Pölsterl, S., Wachinger, C.: Vox2cortex: fast explicit reconstruction of cortical surfaces from 3d mri scans with geometric deep neural networks. In: Proceedings of the IEEE/CVF Conference on Computer Vision and Pattern Recognition, pp. 20773–20783 (2022)
5. Criminisi, A., Sharp, T., Blake, A.: GeoS: geodesic image segmentation. In: Forsyth, D., Torr, P., Zisserman, A. (eds.) *ECCV 2008. LNCS*, vol. 5302, pp. 99–112. Springer, Heidelberg (2008). https://doi.org/10.1007/978-3-540-88682-2_9
6. Defferrard, M., Bresson, X., Vandergheynst, P.: Convolutional neural networks on graphs with fast localized spectral filtering. In: *Advances in Neural Information Processing Systems*, vol. 29 (2016)
7. Gopinath, K., Desrosiers, C., Lombaert, H.: SegRecon: learning joint brain surface reconstruction and segmentation from images. In: de Bruijne, M., et al. (eds.) *MICCAI 2021. LNCS*, vol. 12907, pp. 650–659. Springer, Cham (2021). https://doi.org/10.1007/978-3-030-87234-2_61
8. Govil, S., et al.: A deep learning approach for fully automated cardiac shape modeling in tetralogy of Fallot. *J. Cardiovasc. Magn. Reson.* **25**(1), 15 (2023)

9. Guo, F., Li, M., Ng, M., Wright, G., Pop, M.: Cine and multicontrast late enhanced MRI registration for 3D heart model construction. In: Pop, M., et al. (eds.) STACOM 2018. LNCS, vol. 11395, pp. 49–57. Springer, Cham (2019). https://doi.org/10.1007/978-3-030-12029-0_6
10. Hanocka, R., Metzler, G., Giryes, R., Cohen-Or, D.: Point2mesh: a self-prior for deformable meshes. arXiv preprint [arXiv:2005.11084](https://arxiv.org/abs/2005.11084) (2020)
11. Havsteen, I., Ohlhues, A., Madsen, K.H., Nybing, J.D., Christensen, H., Christensen, A.: Are movement artifacts in magnetic resonance imaging a real problem?—a narrative review. *Front. Neurol.* **8**, 232 (2017)
12. Investigators, S.H.: Coronary CT angiography and 5-year risk of myocardial infarction. *N. Engl. J. Med.* **379**(10), 924–933 (2018)
13. Isensee, F., Jaeger, P.F., Kohl, S.A., Petersen, J., Maier-Hein, K.H.: NNU-net: a self-configuring method for deep learning-based biomedical image segmentation. *Nat. Methods* **18**(2), 203–211 (2021)
14. Kong, F., Shadden, S.C.: Whole heart mesh generation for image-based computational simulations by learning free-from deformations. In: de Bruijne, M., et al. (eds.) MICCAI 2021. LNCS, vol. 12904, pp. 550–559. Springer, Cham (2021). https://doi.org/10.1007/978-3-030-87202-1_53
15. Kong, F., Shadden, S.C.: Learning whole heart mesh generation from patient images for computational simulations. *IEEE Trans. Med. Imaging* **42**, 533–545 (2022)
16. Kramer, C.M., Barkhausen, J., Flamm, S.D., Kim, R.J., Nagel, E.: Standardized cardiovascular magnetic resonance imaging (CMR) protocols, society for cardiovascular magnetic resonance: board of trustees task force on standardized protocols. *J. Cardiovasc. Magn. Reson.* **10**, 1–10 (2008)
17. Lebrat, L., et al.: CorticalFlow: a diffeomorphic mesh transformer network for cortical surface reconstruction. *Adv. Neural. Inf. Process. Syst.* **34**, 29491–29505 (2021)
18. Liao, J.R., Pauly, J.M., Brosnan, T.J., Pelc, N.J.: Reduction of motion artifacts in cine MRI using variable-density spiral trajectories. *Magn. Reson. Med.* **37**(4), 569–575 (1997)
19. Loop, C.: Smooth subdivision surfaces based on triangles (1987)
20. Lorensen, W.E., Cline, H.E.: Marching cubes: a high resolution 3d surface construction algorithm. *ACM SIGGRAPH Comput. Graph.* **21**(4), 163–169 (1987)
21. Ma, Q., Li, L., Robinson, E.C., Kainz, B., Rueckert, D., Alansary, A.: CortexODE: learning cortical surface reconstruction by neural odes. *IEEE Trans. Med. Imaging* **42**, 430–443 (2022)
22. Ma, R., Wang, R., Pizer, S., Rosenman, J., McGill, S.K., Frahm, J.-M.: Real-time 3D reconstruction of colonoscopic surfaces for determining missing regions. In: Shen, D., et al. (eds.) MICCAI 2019. LNCS, vol. 11768, pp. 573–582. Springer, Cham (2019). https://doi.org/10.1007/978-3-030-32254-0_64
23. Menchón-Lara, R.M., Simmross-Wattenberg, F., Casaseca-de-la Higuera, P., Martín-Fernández, M., Alberola-López, C.: Reconstruction techniques for cardiac cine MRI. *Insights Imaging* **10**, 1–16 (2019)
24. Shi, L., Zhang, Y., Cheng, J., Lu, H.: Two-stream adaptive graph convolutional networks for skeleton-based action recognition. In: Proceedings of the IEEE/CVF Conference on Computer Vision and Pattern Recognition, pp. 12026–12035 (2019)
25. Suinesiaputra, A., Gilbert, K., Pontre, B., Young, A.A.: Imaging biomarkers for cardiovascular diseases. In: Handbook of Medical Image Computing and Computer Assisted Intervention, pp. 401–428. Elsevier (2020)

26. Wang, P., Liu, L., Liu, Y., Theobalt, C., Komura, T., Wang, W.: NEUS: learning neural implicit surfaces by volume rendering for multi-view reconstruction. arXiv preprint [arXiv:2106.10689](https://arxiv.org/abs/2106.10689) (2021)
27. Wickramasinghe, U., Remelli, E., Knott, G., Fua, P.: Voxel2Mesh: 3D mesh model generation from volumetric data. In: Martel, A.L., et al. (eds.) MICCAI 2020. LNCS, vol. 12264, pp. 299–308. Springer, Cham (2020). https://doi.org/10.1007/978-3-030-59719-1_30
28. Wolberg, G., Sueylam, H., Ismail, M., Ahmed, K.: One-dimensional resampling with inverse and forward mapping functions. J. Graphics Tools **5**(3), 11–33 (2000)
29. Xu, H., et al.: Whole heart anatomical refinement from CCTA using extrapolation and parcellation. In: Ennis, D.B., Perotti, L.E., Wang, V.Y. (eds.) FIMH 2021. LNCS, vol. 12738, pp. 63–70. Springer, Cham (2021). https://doi.org/10.1007/978-3-030-78710-3_7
30. Yan, S., Xiong, Y., Lin, D.: Spatial temporal graph convolutional networks for skeleton-based action recognition. In: Proceedings of the AAAI Conference on Artificial Intelligence, vol. 32 (2018)